



# Investigation of load alleviation in aircraft pre-design and its influence on structural mass and fatigue

V. Handojo

DLR (German Aerospace Center), 37073 Göttingen, Germany

## ARTICLE INFO

### Article history:

Received 20 May 2021

Received in revised form 3 February 2022

Accepted 7 February 2022

Available online 11 February 2022

Communicated by Grigorios Dimitriadis

### Keywords:

Load alleviation

Loads analysis

Structural optimization

Fatigue analysis

Aircraft pre-design

## ABSTRACT

This work elaborates an aircraft pre-design process that integrates loads analysis, load alleviation, structural optimization and fatigue analysis. The consideration of maneuver and gust load alleviation in early design stages is a promising concept to reduce wing bending moments, structural mass and extend the fatigue life, as shown on two mid-range configurations: one with a backward and another one with a forward swept wing respectively. In the loads analysis, quasi-steady maneuvers and dynamic 1-cos gusts are considered. For the load alleviation, the ailerons are deflected symmetrically. While the maneuver load alleviation reacts to the commanded load factor, the gust load alleviation reacts to fluctuations in the angle of attack. With the selected loads from the simulations, the structure of the wing and horizontal tailplane (HTP) is optimized toward mass minimization. The constraints considered are material strength, buckling stability and static aeroelastic requirements. The steps comprising loads analysis and structure optimization are conducted iteratively until the wing box mass converges. The load alleviation yields a reduction of wing box mass by 2.8% on the backward and 6.1% on the forward swept wing configuration. A subsequent, qualitative fatigue analysis is carried out to compare the fatigue behaviors of the active and passive aircraft (with and without load alleviation). For the reference missions, loads due to continuous turbulence and ground-air-ground cycles are considered, and the fatigue life of the active aircraft is improved by 28% and 12% respectively, on top of the mass benefit. As a conclusion, the proposed process can serve to gain an insight into the effects of load alleviation on the design loads, mass reduction and the resulting change in the fatigue behavior of a given aircraft in the pre-design phase, before it advances to the next design stage.

© 2022 The Author(s). Published by Elsevier Masson SAS. This is an open access article under the CC BY-NC-ND license (<http://creativecommons.org/licenses/by-nc-nd/4.0/>).

## 1. Introduction

The design of new aircraft is a long, complex multidisciplinary process. To minimize the aircraft's development and operational costs, it is advisable to shift as many analyses and calculations as possible to earlier stages of the design.

One solution to lower the aircraft's operational cost is by minimizing the fuel consumption. This can be achieved e.g. by reducing the structural mass. At the same time, the structural mass directly depends on the design loads. Hence, structural mass can be reduced by alleviating the design loads. Nowadays, active load alleviation is implemented on commercial transport aircraft as a part of the electronic flight control system (EFCS) [1]. However, before the load alleviation is well adjusted to the aircraft, it has to be modeled in the design process first – the earlier the better.

In the conceptual stage, empirical regression formulae – including technology factors for load alleviation – are often used since

information about the aircraft is insufficient. In the preliminary design stage, the aircraft configuration is frozen and more details about the aircraft are known. In this case, a physics based modeling of load alleviation systems is seen as appropriate since it can be efficiently integrated into the physics-based loads analysis as shown by this work. With a physics based method, there are more degrees of freedom in setting the load alleviation architecture/parameters to maximize the load reduction. However, the algorithm should be computer-time efficient so that the load calculations, which can comprise hundreds or more load cases, are considerably fast. This large number of load cases argue against the use of high-fidelity methods such as computational fluid dynamics (CFD). Besides, CFD models are not always available for any aircraft in the early design stages.

Regarding previous works in load alleviation, Binder et al. investigated the influences of active aeroelastic control, passive aeroelastic tailoring and their combination on the structural mass of the wing [2]. To achieve the largest mass reduction, maneuver load alleviation (MLA), gust load alleviation (GLA) and aeroelastic tailoring should be implemented simultaneously [2]. Xu et al. shows the

E-mail address: [vega.handojo@dlr.de](mailto:vega.handojo@dlr.de).

influence of load alleviation among others on the reduction of the structural mass and operational cost with a conceptual design process [3]. Paletta investigated the loads and fatigue benefit of load alleviation on a business jet configuration [4]. With load alleviation, the fatigue life is extended by 44-67% [4]. Teufel shows the effects of load alleviation on the gust and turbulence loads, and discusses the influence of 2D turbulence on various load quantities [5]. However, the chain of impact of load alleviation on design loads, structural mass and fatigue has not been addressed. Therefore, to gain insight of the interdependency between those aspects, they are investigated simultaneously in this work. Fig. 1 visualizes the workflow: the influence of load alleviation on the design loads and the structural mass is investigated in an iterative process, and a subsequent fatigue analysis is carried out. This work is based on the dissertation [6]. In the dissertation, further aspects regarding operational aspects of load alleviation and its influence on the structural fatigue are discussed.

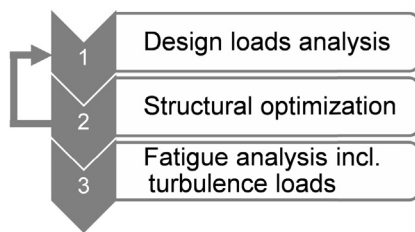


Fig. 1. Global workflow of the investigation.

## 2. Reference aircraft and simulation models

### 2.1. Reference aircraft

Two reference aircraft are investigated: the backward swept D150 configuration and the forward swept ALLEGRA configuration. The D150 configuration [7] is similar to the Airbus A320, a typical mid-range commercial aircraft with aluminum structure, engines mounted under the wing and fuselage mounted empennage.

The ALLEGRA configuration, that originates from the LamAiR configuration [8], is selected as the second reference aircraft. Its parameters such as payload, operating Mach number and design masses are similar to the D150 configuration. ALLEGRA has an unconventional forward swept wing and T-tail configuration and is made of composite materials with fixed ply angle distributions. The configuration aspects are expected to evoke aeroelastic effects that are not observable on the D150 configuration. Fig. 2 and 3 show the geometry of the D150 and ALLEGRA configuration.

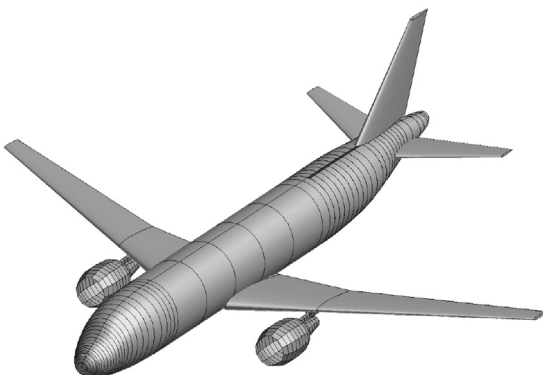


Fig. 2. Geometry of the D150 configuration.

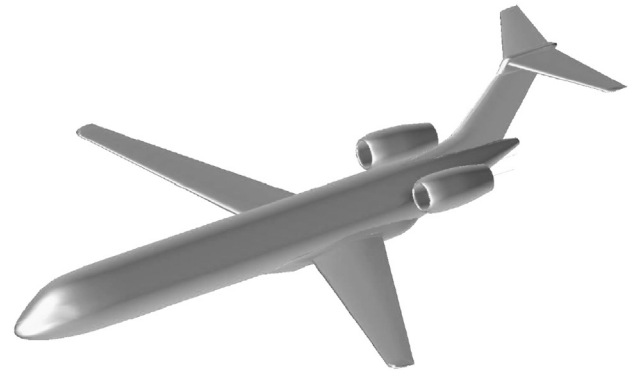


Fig. 3. Geometry of the ALLEGRA configuration.

### 2.2. Simulation models

For the loads analysis and structural optimization, MSC.Nastran models of the reference aircraft generated with the DLR in-house MONA process [9] are used. The primary structure on the lifting surfaces and control surfaces is modeled with shell elements for the spars, skins and ribs, as well as with bar elements for the stiffeners. The fuselage is modeled with beam elements. In the MONA process, the finite element (FE) models undergo a preliminary structural sizing using analytic-empirical methods [10]. Fig. 4 shows the FE model of the D150 configuration, while the shell elements of the fuselage and engines are represented for illustration purpose only.

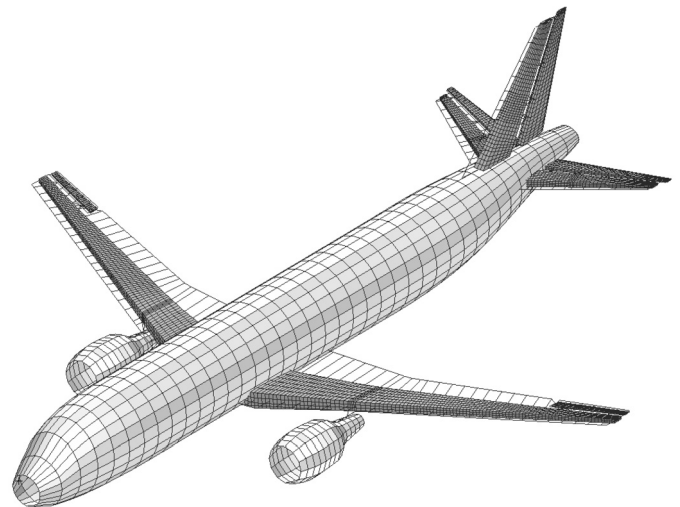


Fig. 4. FE model of the D150 configuration.

The total mass of both aircraft models consists of structural masses, secondary masses, systems, fuel modeled according to Klimmek [10] and payload. To reduce computing time in the loads analysis, the stiffness and mass properties of the reference aircraft are condensed onto the load reference axis (LRA) nodes. Fig. 5 shows those nodes using the triangular markers.

The aerodynamic forces on the lifting surfaces are modeled using the vortex lattice method (VLM) for the steady cases or doublet lattice method (DLM) for the unsteady cases [11,12]. To consider the aerodynamic effect of the fuselage, the subsonic wing-body interference theory is used [13]. Fig. 6 shows the aerodynamic model of the D150 configuration. To consider the aerodynamic effects due to the twist and camber of the wing, a downwash correction with W2GJ matrix [10] created using ModGen is implemented. For transonic flow conditions, a correction of the AIC matrices can be

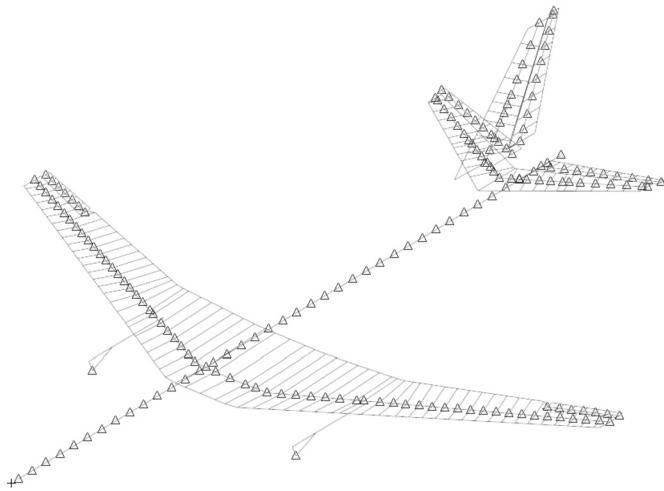


Fig. 5. Condensed FE model of the D150 configuration.

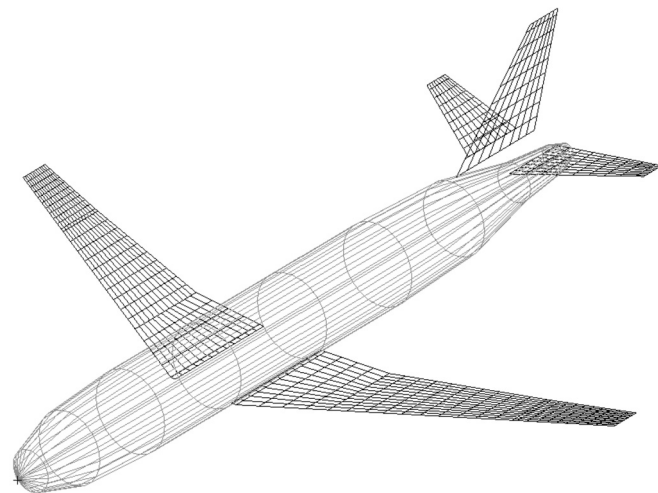


Fig. 6. Aerodynamic model of the D150 configuration.

considered, for example using data from CFD. However, CFD models are not always available in the early stages of the aircraft design process, so that CFD based corrections are not always possible.

### 3. Design process of loads analysis and structural optimization

This section describes the steps conducted in the design process.

#### 3.1. Loads analysis

The loads analysis part considers symmetric maneuvers (+2.5 g pull-ups and -1.0 g push-downs) and vertical 1-cos gusts with gust gradients ranging from 9 to 107 m according to CS25 [14]. The maneuver and gust simulations are carried out with the elastic aircraft using MSC.Nastran [12] (SOL144 and SOL146 respectively). The maneuver loads are calculated in quasi-steady equilibria with the prescribed load factors  $n_z$  and pitching rate  $q$ :

$$q = \frac{(n_z - 1) \cdot g}{V_{TAS}}, \quad (1)$$

with the gravitational acceleration  $g$  and the aircraft true airspeed  $V_{TAS}$ .

The dynamic gust loads are calculated in the frequency domain with a maximum analysis frequency  $f_{max}$  of 50 Hz. Regarding the

unsteady aerodynamics, reduced frequencies up to 1.0 are considered. The reduced frequency  $k$  is defined by:

$$k = \frac{2\pi f \cdot \bar{c}}{2V_{TAS}}, \quad (2)$$

with the frequency  $f$  and the reference chord  $\bar{c}$ . With the flight parameters of the reference aircraft, a reduced frequency of 1.0, as stated in Equation (2), is equivalent to a frequency of up to 20 Hz. This is seen as sufficient since more than 99% of the energy of 1-cos gusts is contained in frequencies up to twice of the gust base frequency  $f_g$  defined by:

$$f_g = \frac{V_{TAS}}{2 \cdot H}, \quad (3)$$

with the gust gradient  $H$ . Gust base frequencies, that are potentially relevant for the structural optimization, are expected to be close to the first wing bending frequency. For commercial transport aircraft, the first wing bending mode typically occurs between 1 Hz and 5 Hz, depending on the aircraft geometry and mass configuration. As a conclusion, unsteady aerodynamics for frequencies up to 10 Hz are seen as sufficient for the gust loads analysis.

The calculated gust loads represent the incremental loads only. Thus, to obtain the total loads, the gust loads have to be superposed with the corresponding 1 g trim loads.

Remark: continuous turbulence is not included in the limit load calculations, since the equations in CS25.341(b) [14] yield curves of equal probability of occurrence instead of time-correlated loads. The latter are necessary for structural optimizations with MSC.Nastran. Mathematically, it is possible to generate concrete time-correlated loads with continuous turbulence, e.g. using a random phase distribution, see Section 5. However, this method is not suitable for limit load calculations, since the maximum values of the loads might change unpredictably, depending on the phase distribution. On the other hand, for fatigue loads analysis as described in Section 5, the load histogram (load amplitude distribution) is more important, and it stays more constant regardless of the phase distribution. Hence, time-correlated loads with continuous turbulence are seen to be more suitable for fatigue analysis instead of limit load calculations.

Following the maneuver and gust simulations, the loads are post-processed to identify the relevant load cases for the structural optimization using 2D load envelopes with the combination  $M_x/M_y$  and  $M_x/F_z$ . The 2D envelopes are generated at six span positions on the wing and two positions on the HTP. Fig. 7 shows an exemplary 2D envelope. The load cases appearing on the edges of the 2D envelopes comprise the loads considered in the structural optimization.

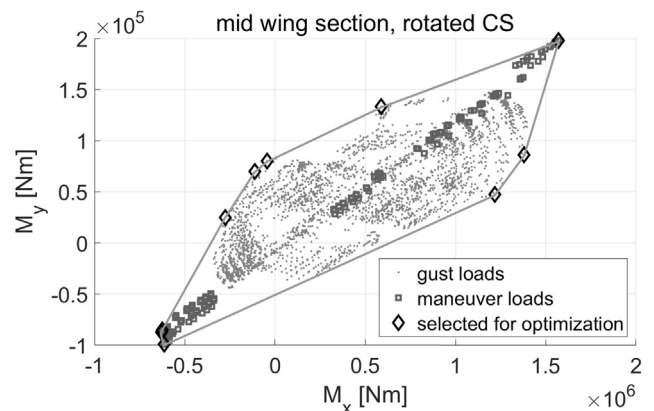


Fig. 7. 2D envelope surrounding gust and maneuver loads.

### 3.2. Structural optimization

With the post-processed loads, the structure of the wing and the HTP is optimized using SOL200 of MSC.Nastran [15] that implements gradient-based algorithms. The considered constraints are material strength, buckling stability and minimum thickness that are described in more detail in Section 6. Within the optimization run, the structure is updated iteratively until the convergence criterion is satisfied. For the D150 configuration, the defined convergence criterion is a relative mass change of  $5.0 \cdot 10^{-4}$  between two design iterations, while a relative mass change of  $1.0 \cdot 10^{-3}$  is set for the ALLEGRA configuration due to its non-isotropic material properties and thus longer computing time within the structural optimization. The objective of the structural optimization lies in minimizing the structural mass while complying with the constraints under the applied loads, and the design variables are the material thicknesses - also for the composite ALLEGRA wing, since the ply angle distributions on the skins, spars and ribs are kept constant.

The resulting design is then inputted into a subsequent optimization with aeroelastic constraints since it is faster to solve multiple, smaller optimization problems compared to a large one. On the D150 configuration, the considered constraint is the aileron effectiveness that has to stay positive at speeds up to  $V_D + 15\%$  according to CS25.629 [14]. On the forward swept ALLEGRA configuration, the design has to be free of torsional divergence at speeds up to  $V_D + 15\%$ . If the aeroelastic constraints are not satisfied, the wing is re-optimized and only an increase of the material thicknesses is allowed [10].

### 3.3. Workflow

Fig. 8 visualizes the workflow with the loads analysis and structural optimization. With the initial presized design from ModGen, the steps comprising the loads analysis (3 to 6) and the structural optimization (7 to 9) are conducted iteratively until the relative change in wing structural mass between two cycles of loads and optimization is below 0.5%. Subsequently, a subsonic flutter check is carried out to ensure that the aircraft does not flutter in the prescribed range of dynamic pressure.

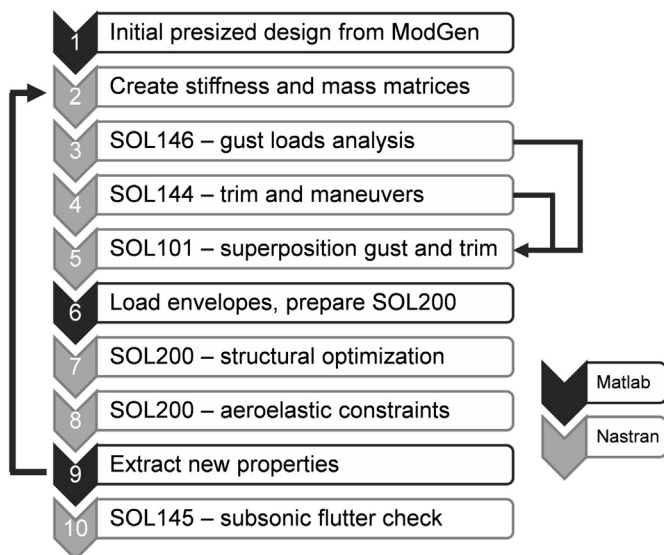


Fig. 8. Workflow of loads analysis and structural optimization.

## 4. Load alleviation functions

The considered load alleviation functions comprise maneuver and gust load alleviation.

### 4.1. Maneuver load alleviation

The maneuver load alleviation (MLA) is carried out by deflecting the ailerons symmetrically (aileron deflection is denoted as  $\xi$ ). To avoid interference with the flight mechanic controller, the MLA should only react to the commanded load factor. The aileron deflection for MLA is set to  $-8^\circ$  (trailing edge up) at the design cruise speed  $V_C$  and a load factor of 2.5. To achieve a more constant load alleviation effect in the entire flight envelope, the MLA amplitude  $\xi_{MLA}$  is set inversely proportional to the dynamic pressure  $\bar{q}$ . In addition, the MLA amplitude is set proportional to the commanded load factor deviation  $(n_{z,c} - 1.0)$ , so that the following algorithm results:

$$\xi_{MLA}(\bar{q}, n_{z,c}) = \begin{cases} -8^\circ \cdot \frac{\bar{q}_C}{\bar{q}} \cdot \frac{n_{z,c} - 1.0}{n_{z,max} - 1.0} & \text{for } n_{z,c} > 1 \\ -8^\circ \cdot \frac{\bar{q}_C}{\bar{q}} \cdot \frac{n_{z,c} - 1.0}{1.0 - n_{z,min}} & \text{for } n_{z,c} < 1 \end{cases}, \quad (4)$$

with the commanded load factor  $n_{z,c}$ , the maximum design load factor  $n_{z,max}$  of 2.5, the minimum design load factor  $n_{z,min}$  of -1.0 and the dynamic pressure at the design cruise speed  $\bar{q}_C$ .

As an example: at the maneuvering speed  $V_A$  of the D150, where the dynamic pressure is low with  $\bar{q}_A \approx 0.52 \bar{q}_C$ , the MLA deflection at 2.5 g is  $-15^\circ$ . This value is comparable to the MLA of the Lockheed L-1011 ( $-13^\circ$  at 2.5 g) [16].

### 4.2. Gust load alleviation

Analogous to the MLA, the gust load alleviation (GLA) is carried out by deflecting the ailerons symmetrically. The main input for the controller comes from the aerodynamic sensors that are assumed to be located at the aircraft nose. To filter out flight mechanical effects on the aerodynamic data, the gust angle of attack  $\alpha_g$  as defined by König et al. [17] is considered in the control algorithm:

$$\alpha_g = \alpha_m - \theta + \frac{\dot{z}}{V_{TAS}} + \frac{q \cdot r_{CG}}{V_{TAS}} \approx \frac{w_g}{V_{TAS}}, \quad (5)$$

with the measured angle of attack  $\alpha_m$ , the aircraft pitch angle  $\theta$ , the aircraft vertical speed  $\dot{z}$ , the aircraft true airspeed  $V_{TAS}$ , the aircraft pitch rate  $q$ , the distance between aerodynamic sensor and aircraft CG  $r_{CG}$  and the vertical wind speed  $w_g$ .

For the first step, the symmetric aileron deflection is set proportional to the gust angle of attack. The gain is set to  $\frac{-2.0}{\cos \phi_{hinge}}$  where  $\phi_{hinge}$  is the sweep angle of the control surface hinge. The correction for the hinge sweep angle is necessary, since the actuator deflection is always larger than the aerodynamic deflection of a swept control surface. As an example: for a control surface with  $45^\circ$  sweep angle, an actuator deflection of  $1.0^\circ$  would yield an aerodynamic deflection of only  $\cos(45^\circ) \cdot 1.0^\circ \approx 0.71^\circ$ . The selected gain is based on the potential theory of an unswept wing [18]: for a trailing edge control surface with a relative chord of 0.25 and an aerodynamic effectiveness of 0.75, a control surface (aerodynamic) deflection of  $-2.0^\circ$  would compensate the lift due to a change in the angle of attack of  $1.0^\circ$ .

Since discrete gust encounters are transient phenomena and the maximum loads are reached within a second after the gust is detected at the aircraft nose, an integral term is not necessary. A second-order low pass filter for the GLA is set at 10 Hz to avoid excessive aileron deflection rates. To avoid having aileron deflection

in a constant vertical wind field, a second-order high-pass filter is set at 0.1 Hz.

Concerning the delay time  $t_{del}$ , the flight control computer is assumed to process the angle of attack signal measured at the nose and output the aileron deflection command when the gust arrives at the wing, while a minimum delay time of 60 ms – as applied by Wildschek [19] – is considered for the computing time:

$$t_{del} = \max\left(\frac{x_{wing}}{V_{TAS}}, 0.06 \text{ s}\right), \quad (6)$$

where  $x_{wing}$  is the x-position of the wing. However, the latter is not exactly defined yet. By trying out different positions for  $x_{wing}$ , it turns out that setting it to 16 m on D150 and 18 m on ALLEGRA yields the largest reduction of the wing root bending moment. Fig. 9 and 10 visualize the two positions, and it is apparent that the ailerons should start deflecting relatively soon after the gust hits the foremost leading edge of the wing.

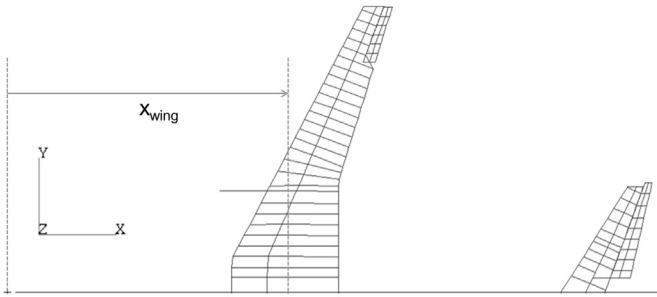


Fig. 9. Reference position  $x_{wing}$  on the D150 configuration.

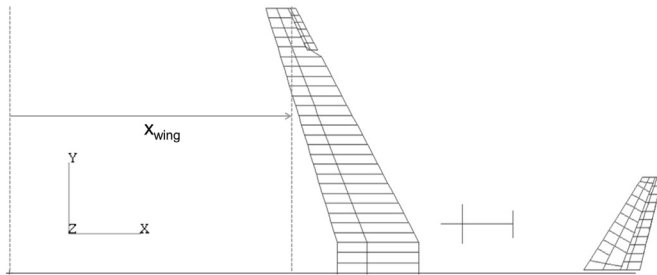


Fig. 10. Reference position  $x_{wing}$  on the ALLEGRA configuration.

Thus, the GLA transfer function  $TF_{GLA}$  is:

$$TF_{GLA}(f) = \frac{\xi_{c, GLA}}{\alpha_g} = k_{GLA} \cdot TF_{LP} \cdot TF_{HP} \cdot TF_{del}, \quad (7)$$

with:

$$TF_{del} = e^{-2\pi \cdot if \cdot t_{del}}, \quad (8)$$

and the commanded aileron deflection  $\xi_{c, GLA}$ , the frequency  $f$ , the GLA gain  $k_{GLA} = \frac{-2.0}{\cos\phi_{hinge}}$ , the second order low pass  $TF_{LP}$  at 10 Hz, the second order high pass  $TF_{HP}$  at 0.1 Hz and the transfer function of the delay time  $TF_{del}$ .

The term commanded deflection implies that the time domain rate limiter is not applied yet. For the actual aileron deflection, a rate limiter at  $40^\circ/s$  is implemented. This step requires a transformation of the aileron deflection into the time domain, and after the rate limiter is applied, the aileron deflection is transformed back into the frequency domain.

## 5. Turbulence loads and fatigue analysis

For the fatigue analysis, the considered loading conditions are turbulence loads and ground-air-ground cycles.

### 5.1. Turbulence loads

For the first step, a reference flight mission along with its parameters is defined. To evoke the largest loads on the wing, the aircraft are assumed to carry the maximum payload, and fuel is added until the maximum take-off mass (MTOM) is approximately reached. The fueling sequence is outer tank – inner tank – center tank. With the available fuel mass, the longest possible routes are searched using fuelplanner [20] to estimate the duration of each reference flight phase (climb, cruise, descent). In doing so, the fuel consumption estimation is based on the A320 and the JAR international standard [21] is considered for the reserve fuel mass. The D150 is assigned for the route from Berlin-Tegel (EDDT) to Porto (LPPR), while the route Berlin-Tegel (EDDT)-Athens International (LGAV) is selected for the ALLEGRA configuration. More details regarding the fuel masses can be found in Section 6 and 7.

During the reference mission, the aircraft are assumed to fly in continuous turbulence that has the von Kármán spectrum and a scale of turbulence of 762 m (2500 ft) as prescribed in CS25.341(b)(2) [14]. For each flight phase, a reference root mean square (RMS) of the vertical wind speed is defined. It is assumed that the turbulence intensity is moderate such that the probability of exceedance of the RMS is approximately  $10^{-3}$  according to MIL-STD-1797A [22]. The nominal values of the RMS are listed in Section 6.

Since the turbulence spectrum  $\Phi(f)$  is given in the power spectral density form while the vertical wind speed  $w_{g, turb}(f)$  is necessary for the aircraft response calculation, the latter is calculated by:

$$w_{g, turb}(f) = \sqrt{(\Phi(f) \cdot f_{max} \cdot 2n_f)} \cdot e^{i \cdot \text{rand}(\varphi(f))}, \quad (9)$$

with the maximum analysis frequency  $f_{max}$  of 50 Hz, the number of frequency samples  $n_f$  of  $5 \cdot 10^4$  and the random phase angle  $\text{rand}(\varphi(f))$ . The selected  $f_{max}$  of 50 Hz is analogous to the dynamic gust simulations, and  $n_f$  of  $5 \cdot 10^4$  is seen as adequate to generate statistically relevant load collectives without requiring excessive memory and performance for the computation.

With the vertical speed in the frequency domain, the aircraft response is calculated using transfer functions (TF) that are calculated using SOL146 of MSC.Nastran. In doing so, the input quantities are unit vertical wind speed and unit aileron deflection, while the main output quantities for the fatigue analysis are the major principal stresses/strains of selected structure elements on the lower wing skin.

For the active aircraft, the GLA algorithm from Equation (7) and a rate limiter at  $40^\circ/s$  (see Subsection 4.2) are considered. Thus, the aircraft response in the frequency domain  $x(f)$  is calculated by:

$$x(f) = TF_{w_g \rightarrow x}(f) \cdot w_g(f) + TF_{\xi \rightarrow x}(f) \cdot \xi(f), \quad (10)$$

with the transfer function with vertical wind as input  $TF_{w_g \rightarrow x}(f)$  and another one with aileron deflection as input  $TF_{\xi \rightarrow x}(f)$ . In general, the aircraft response  $x(f)$  itself can contain any quantity, such as the wing root bending moment, the major principal stress of a wing element, or the acceleration of the wing tip, depending on the aim of the transfer function calculation.

Subsequently, the responses are transformed into the time domain and a rainflow-counting algorithm [23] is applied to derive load collectives based on the aircraft response in the turbulence.

## 5.2. Ground-air-ground cycles

Since ground-air-ground cyclic loads are relevant for the structure fatigue [24], a simplified ground-air-ground cycle is also considered. The aircraft is assumed to have zero stress on the ground, and the stresses during flight are taken from a reference +1.3 g maneuver calculation. The load factor of 1.3 should represent the typical maximum load factor reached in a flight mission, particularly during take-off [25]. The focus of the fatigue analysis is the major principal stress on the lower skin of the wing and the HTP. Therefore, landing cases are not considered since large parts of the lower skin are loaded with compressive stress during the impact. Moreover, +1.15 g turns – which correspond to 30° bank angle – are seen as irrelevant since the load factor fluctuation is only 0.15 g, compared to 1.3 g during the ground-air-ground cycle.

For the 1.3 g maneuver simulation, the aircraft are assumed to have the take-off mass according to Subsection 5.1, and the flight condition of the climb phase is considered, see Table 1. The climb condition is selected instead of the take-off condition since the high-lift systems are not modeled. For the active aircraft, Equation (4) yields an MLA deflection of -2.5° for the active aircraft.

**Table 1**  
Parameters of the climb condition.

Parameter	Value
Altitude	4572 m (FL150)
Airspeed	181.6 m/s TAS (280 KEAS)
Mach number	0.563
Dynamic pressure	12700 Pa
Load factor	1.3

With the assumption that the aircraft has zero stress on the ground, the stresses during the +1.3 g maneuver represent the peak-to-peak differences in a ground-air-ground cycle. Thus, the stress amplitudes considered in the fatigue damage calculation are half of those stresses during the +1.3 g maneuver.

## 5.3. Fatigue damage accumulation

For the linear fatigue damage accumulation, the Palmgren-Miner's rule [26] is applied. With a given S-N (stress-cycle) curve for the respective material and stress ratio, the fatigue damage per hour  $D_F/h$  is accumulated as follows:

$$D_F/h = \sum_i \frac{n_i/h}{N_i} \quad (11)$$

with the index  $i$  for the stress amplitude classes, the number of load cycles per hour for the respective amplitude class  $n_i/h$ , and the fatigue life limit of the respective amplitude derived from S-N curves  $N_i$ . While this method is commonly used for metal fatigue, it is also taken as a first approximation for composite fatigue. The considered S-N curves are described in Section 6 and 7.

## 6. Results - D150 configuration

### 6.1. Parameter space

For the loads analysis part, nine mass configurations ranging from the operating empty mass (OEM) to the MTOM covering center of gravity (CG) positions between 13% and 42% of the reference chord are considered. For the flight conditions, three altitudes between 0 m and 7000 m are taken into account. The latter is the altitude where  $V_C$  coincides with  $M_C$ .

In the 1-cos gust simulations, seven gust gradients ranging from 9 to 107 m (30 to 350 ft) are considered, and the gust speeds

are calculated according to CS25.341 [14]. The largest gust loads tend to emerge at  $V_C$  and altitudes between 0 m and  $Z(V_C = M_C)$  because there the combination between the highest dynamic pressures and the highest gust speeds is found. Thus, only flight conditions at  $V_C$  are taken into account. With nine mass configurations, three altitudes, seven gust gradients and two gust directions – vertical upward and downward – each, a total of 378 gust cases are included in the loads analysis.

The maneuver simulations cover symmetrical 2.5 g pull-ups and -1.0 g push-downs. The pull-up maneuvers are calculated at  $V_A$  and  $V_D$ , while the push-downs are simulated at  $V_A$  (instead of  $V_H$  to simplify the airspeed calculations) and  $V_C$ .  $V_H$  is the stall speed when performing a -1.0 g push-down. With nine mass configurations, three altitudes and four maneuvers each, there are 108 maneuver cases that are considered.

In the structural optimization, the strength constraint is the von-Mises stress (441 MPa ultimate stress for the aluminum). The buckling stability constraint is represented by simplified two-dimensional buckling phenomena as applied by Klimmek [10]:

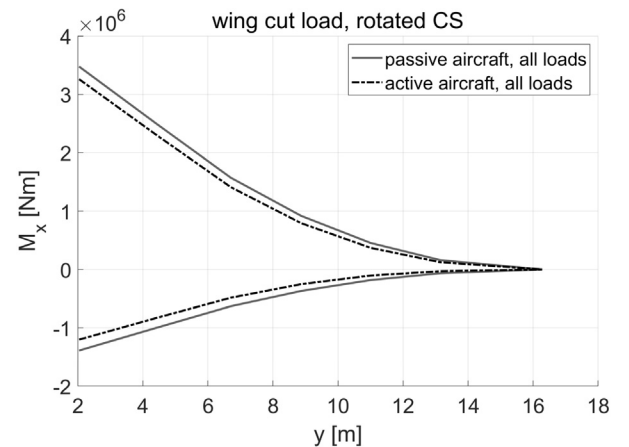
$$\sigma_{bc} = \frac{\pi^2 k_c E}{12(1 - \nu^2)} \left( \frac{t}{b} \right)^2, \quad (12)$$

with the compressive buckling stress  $\sigma_{bc}$ , the compressive buckling coefficient  $k_c$ , the tensile modulus  $E$ , the Poisson ratio  $\nu$ , the material thickness  $t$  and the buckling field width  $b$  that is the distance between two stringers.

In addition, a minimum skin thickness of 2 mm is considered. Regarding the aeroelastic stability, the aileron effectiveness  $\frac{c_{l\xi}(\text{elastic})}{c_{l\xi}(\text{rigid})}$  has to be positive at  $V_D/M_D+15\%$ , where  $c_{l\xi}$  is the rolling moment induced by an aileron deflection.

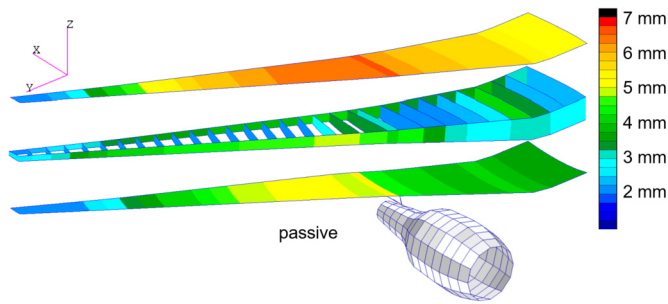
### 6.2. Design loads and structural masses

Fig. 11 visualizes the resulting wing bending moment envelopes of the D150 configuration after ten cycles of loads analysis and structural optimization. The active aircraft (with load alleviation) shows lower wing bending moment values along the half span, and it has 6.2% less bending moment at the root compared to the passive counterpart. In both cases, the largest bending moments are reached during maneuvers.



**Fig. 11.** Bending moment envelope - D150.

Regarding the structural mass, the wing box of the active aircraft is 2.8% lighter compared to the passive aircraft, whereas the difference in the HTP mass is negligible (<1 kg). Fig. 12 and 13 show the thickness distribution on the wing box. On the upper skin of the passive aircraft, the area with a thickness around 6.5



**Fig. 12.** Wing box thickness distribution of the passive D150. (For interpretation of the colors in the figure(s), the reader is referred to the web version of this article.)

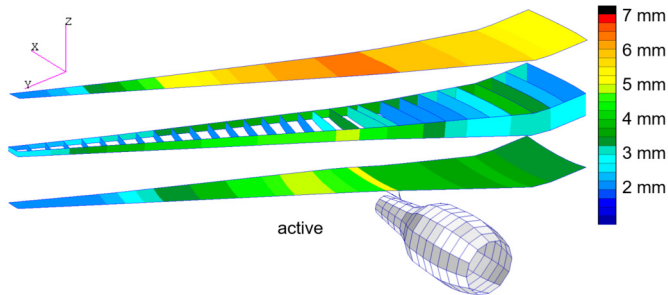


**Fig. 13.** Wing box thickness distribution of the active D150.

mm in the middle wing section is larger compared to the active aircraft. On the lower skin, a larger patch with thicknesses around 5.0 mm is visible on the passive aircraft. Near the wing root, the lower skin of the passive aircraft is approx. 0.2 mm thicker that is explained by the higher wing bending moment magnitude compared to the active aircraft. Near the wing tip, the area with the minimum thickness on the lower skin of the passive aircraft is also smaller.

The wing box mass difference of 2.8% would be equal to 90 kg if only ideal load-carrying masses are considered (no additional masses due to joints, fasteners, access holes and their reinforcements). According to Pinho Chiozzotto [27], an empirical mass factor of 1.45, that is multiplied with the obtained wing box masses, delivers a reliable estimate for the total wing box mass. Hence, with a mass factor of 1.45, the wing mass difference between the active and passive aircraft would be  $1.45 \cdot 90 \text{ kg} = 130.5 \text{ kg}$ , assuming that the secondary masses comprising the systems remain unchanged.

Regarding the aeroelastic constraints, both aircraft do not show aileron reversal nor flutter problems at airspeeds up to  $V_D/M_D + 15\%$ .

### 6.3. Turbulence loads and fatigue analysis

For the route EDDT-LPPR, the great circle distance is 2076 km and the zero fuel mass of the aircraft is 60548 kg. With the take-off fuel of 10450 kg and the trip fuel of 7736 kg obtained using fuelplanner [20], the remaining fuel mass for each flight phase is estimated. Table 2 lists the parameters for each flight phase for the turbulence loads calculation.

For the fatigue analysis, two shell elements on the wing lower skin are monitored: one is located at the root (50% wing box chord) and the other at around 70% span (50% wing box chord). These positions are selected to gain an insight into the fatigue behavior at different positions on the wing. Fig. 14 shows exemplary collectives of the major principal stress during the climb phase. It is apparent that the active aircraft shows lower stress amplitudes: up to 21% at the root and up to 39% at the outer section. In addi-

**Table 2**

Parameters of each flight phase - D150.

Flight phase	Parameter	Value
Climb	Altitude	FL150
	Airspeed	280 KEAS
	Fuel mass	10086 kg
	Turbulence RMS	2.743 m/s TAS
	Duration per flight	0.4 hours
Cruise	Altitude	FL350
	Airspeed	Mach 0.78
	Fuel mass	6456 kg
	Turbulence RMS	1.372 m/s TAS
	Duration per flight	2.0 hours
Descent	Altitude	FL040
	Airspeed	250 KEAS
	Fuel mass	2826 kg
	Turbulence RMS	3.048 m/s TAS
	Duration per flight	0.5 hours

tion, to monitor the effect of load alleviation on HTP fatigue, a shell element at the HTP root (50% HTP box chord) is also observed.

To quantify the fatigue damage, S-N curves from a fatigue experiment campaign by Mayer et al. [28] are taken as reference, and following assumptions are made:

- S-N curves with a stress ratio of 0.1 are considered, because: during the 1 g-flight, the major principal stress at the observed element at the root is 88 MPa. According to Fig. 14, the maximum amplitude of the major principal stress during turbulence is 50 MPa. This yields a stress ratio of  $(88 \text{ MPa} - 50 \text{ MPa}) / (88 \text{ MPa} + 50 \text{ MPa}) = 0.28$ . Furthermore, the stress ratio for ground-air-ground cycles is assumed to be 0.0, see Subsection 5.2. For these reasons, S-N curves with a stress ratio of 0.1 are seen as an acceptable compromise.
- Since the stress amplitudes in the collectives are below 70 MPa, the respective S-N curve approximation function for amplitudes below 70 MPa is selected and extrapolated towards higher number of cycles.
- A fatigue limit is not considered. This means, there is a finite number of cycles to failure for every stress amplitude.
- Since a scatter of cycle numbers, at which failure occurs, is observed in the fatigue experiments, a safety factor of 10 is assumed for the stress cycles to failure.
- Stress amplifications due to structural discontinuities are not considered since the FE-models are optimized without considering those aspects.

With those assumptions, the approximation function for the S-N curve is:

$$N_f = C \cdot \left( \frac{\sigma_{1,a}}{1 \text{ Pa}} \right)^{-n} \cdot \frac{1}{F_S}, \quad (13)$$

with the number of cycles to failure  $N_f$ , the S-N curve constant  $C$  of  $1.31 \cdot 10^{66}$ , the major principal stress amplitude  $\sigma_{1,a}$ , the S-N curve exponent  $n$  of 30.69 and the safety factor  $F_S$ .

Table 3 lists the fatigue damage values induced by turbulence in one reference flight mission according to Table 2. Table 4 lists the fatigue damage per ground-air-ground cycle derived from the loads during a +1.3 g maneuver (see Subsection 5.2). To acquire the total fatigue damage in one flight, the values from Table 3 and Table 4 are added, and Table 5 shows the sums.

With the fatigue damage values in Table 3, Table 4 and Table 5, it is concluded that:

- In turbulence, there is a clear trend that the wing of the passive aircraft shows significantly more fatigue damage compared to the active aircraft. On the other hand, the HTP of the

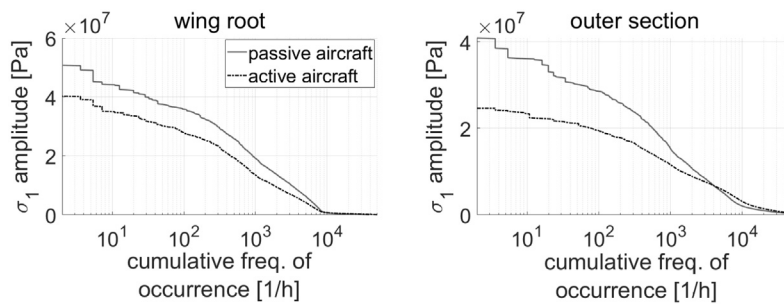


Fig. 14. Stress collectives of D150 during climb.

Table 3

Turbulence fatigue damage per flight - D150.

Observed shell element	Damage per flight:	
	passive aircraft	active aircraft
Wing root	$2.15 \cdot 10^{-12}$	$9.97 \cdot 10^{-15}$
Outer section	$1.05 \cdot 10^{-15}$	$4.19 \cdot 10^{-21}$
HTP root	$2.67 \cdot 10^{-21}$	$4.58 \cdot 10^{-21}$

Table 4

Fatigue damage per ground-air-ground cycle - D150.

Observed shell element	Damage per flight:	
	passive aircraft	active aircraft
Wing root	$5.48 \cdot 10^{-12}$	$5.93 \cdot 10^{-12}$
Outer section	$3.25 \cdot 10^{-12}$	$5.70 \cdot 10^{-12}$
HTP root	$3.10 \cdot 10^{-28}$	$2.10 \cdot 10^{-27}$

Table 5

Fatigue damage per flight cycle - D150.

Observed shell element	Damage per flight:	
	passive aircraft	active aircraft
Wing root	$7.62 \cdot 10^{-12}$	$5.94 \cdot 10^{-12}$
Outer section	$3.25 \cdot 10^{-12}$	$5.70 \cdot 10^{-12}$
HTP root	$2.67 \cdot 10^{-21}$	$4.58 \cdot 10^{-21}$

active aircraft exhibits slightly more damage. This is caused by the GLA creating a small amount of additional pitching moment due to the aileron deflections. Hence, the root mean square of the pitching acceleration on the active aircraft is up to 8.4% higher. This induces additional vertical movements and also loads on the HTP.

- One ground-air-ground cycle tends to cause more wing fatigue damage to the active aircraft than to the passive aircraft, although the active aircraft already uses MLA. This means, if the aircraft only flew through calm air with no turbulence throughout their service life, the active aircraft would reach its fatigue limit earlier compared to the passive counterpart.
- On both aircraft, the wing receives more fatigue damage from the ground-air-ground cycle compared to turbulence. On the passive aircraft, the ground-air-ground cycle makes up to 72% of the total fatigue damage. On the active aircraft, the ground-air-ground cycle causes more than 99% of the total fatigue damage.
- Due to the higher stress amplitudes in general, the wing root receives more fatigue damage compared to the outer wing section.
- Judging by the highest damage values of each aircraft (the largest numbers in every column in Table 5) with  $7.62 \cdot 10^{-12}$  on the passive and  $5.94 \cdot 10^{-12}$  on the active aircraft, the expected fatigue life of the active aircraft is 1.28 times longer than that of the passive aircraft.

If the fatigue damage values listed in Table 5 are extrapolated to e.g. 40000 flight cycles, those are still significantly below 1.0. The extrapolation is valid with the assumption that the turbulence intensity is equal to the values in Table 2 and there is no stress amplification due to structural discontinuities that can significantly increase the fatigue damage values.

## 7. Results - ALLEGRA configuration

### 7.1. Parameter space

The parameter space for the ALLEGRA configuration is defined analogous to the D150 configuration (see Subsection 6.1) in general.

A total of nine mass configurations between the OEM and MTOM are considered, with the CG position ranging between 10% and 35% of the reference chord. The flight conditions, maneuver and gust load cases are analogous to the D150 configuration. Regarding the constraints in the structural optimization, von-Mises strain is considered instead of stress ( $5 \cdot 10^{-3}$  for ultimate loads, as based on IJsselmuiden for a composite rib design [29]), and the compressive buckling stress according to Tetlow  $\sigma_{bcT}$  [30] is taken:

$$\sigma_{bcT} = \frac{\pi}{6\lambda} \left( \sqrt{E_{11}E_{22}} + \frac{\nu_{12}E_{22}}{2} + \frac{\nu_{21}E_{11}}{2} + 2\lambda G_{12} \right) \left( \frac{t}{b} \right)^2, \tag{14}$$

with:

$$\lambda = 1 - \nu_{12}\nu_{21}, \tag{15}$$

and the longitudinal tensile modulus  $E_{11}$ , the lateral tensile modulus  $E_{22}$ , the Poisson ratios  $\nu_{12}$ ,  $\nu_{21}$ , the shear modulus  $G_{12}$ , the material thickness  $t$  and the buckling field width  $b$ .

### 7.2. Design loads and structural masses

Fig. 15 shows the wing bending moment envelopes of the ALLEGRA configuration after seven cycles of loads analysis and structural optimization. The active aircraft shows lower levels of wing bending moment compared to the passive aircraft, and the difference at the root is 10.7%. The largest bending moments on the passive aircraft are reached during gust encounters, while maneuvers yield the largest bending moments on the active aircraft.

Concerning the structural mass, the wing box of the active aircraft is 6.1% lighter compared to the passive counterpart, while the difference in the HTP mass is negligible (<1 kg). Fig. 16 and 17 visualize the wing box thickness distribution. On the upper and lower skin of the passive aircraft, the areas with 18 mm thickness around the root are larger compared to the active aircraft. In the outer part, the skin areas with the minimum thickness are smaller on the passive aircraft. This indicates that the outer wing section

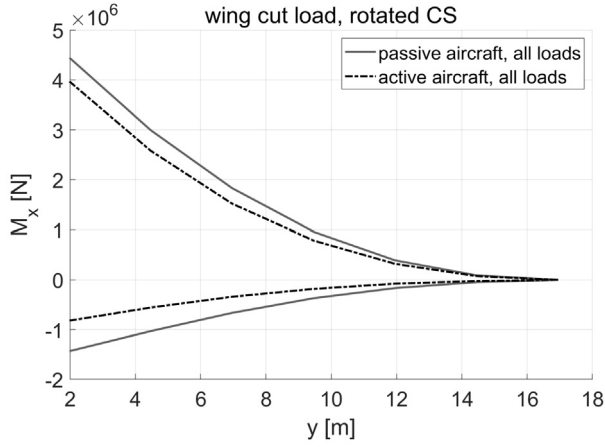


Fig. 15. Bending moment envelope - ALLEGRA.

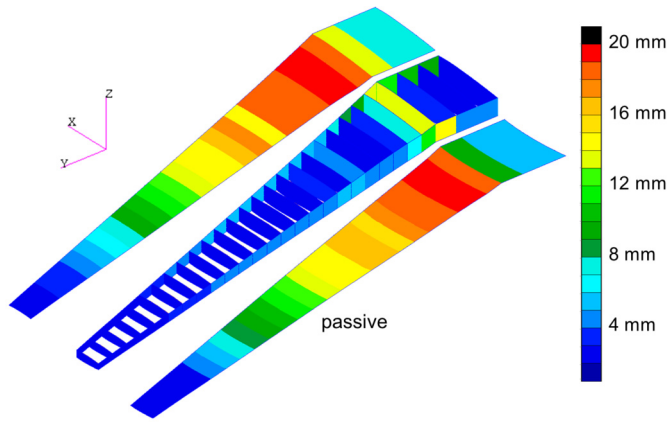


Fig. 16. Wing box thickness distribution of the passive ALLEGRA.

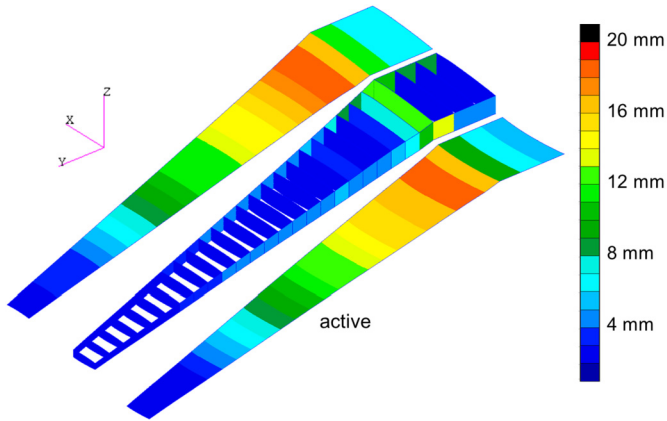


Fig. 17. Wing box thickness distribution of the active ALLEGRA.

of the passive aircraft is more heavily loaded due to the absence of load alleviation.

The difference of 6.1% would be equal to 283 kg on an ideal structure. With the mass factor of 1.45 (see Subsection 6.2), the mass reduction on the active aircraft would be 410 kg.

Regarding the aeroelastic constraints, both aircraft do not show divergence nor flutter problems at airspeeds up to  $V_D/M_D+15\%$ .

### 7.3. Turbulence loads and fatigue analysis

The route EDDT-LGAV has a great circle distance of 1823 km and the zero fuel mass of the aircraft for the mission is 62962 kg.

Table 6

Parameters of each flight phase - ALLEGRA.

Flight phase	Parameter	Value
Climb	Altitude	FL150
	Airspeed	280 KEAS
	Fuel mass	9010 kg
	Turbulence RMS	2.743 m/s TAS
	Duration per flight	0.4 hours
Cruise	Altitude	FL350
	Airspeed	Mach 0.78
	Fuel mass	5892 kg
	Turbulence RMS	1.372 m/s TAS
	Duration per flight	1.8 hours
Descent	Altitude	FL040
	Airspeed	250 KEAS
	Fuel mass	2810 kg
	Turbulence RMS	3.048 m/s TAS
	Duration per flight	0.5 hours

Table 6 lists the parameters for each flight phase for the turbulence loads calculation, and the respective fuel masses are estimated analogous to the D150 configuration.

Analogous to D150, two shell elements on the wing lower skin are monitored in the fatigue analysis: one is located at the root (50% wing box chord) and the other at around 70% span (50% wing box chord). Fig. 18 shows exemplary strain collectives during the climb phase. The active aircraft shows lower strain amplitudes up to 17% at the root and up to 23% at the outer section. In addition, a shell element at the HTP root (50% HTP box chord) is also observed.

To quantify the fatigue damage, reference S-N curves of IM7 composite approximated by Tan et al. [31] are applied with:

$$\frac{\sigma_{max}}{\sigma_{ult}} = 1.037 \cdot N_f^{-0.03269}, \quad (16)$$

with the ratio between maximum stress and ultimate tensile stress  $\frac{\sigma_{max}}{\sigma_{ult}}$  and the number of cycles to failure  $N_f$ .

In the damage accumulation, following assumptions are made:

- The ratio between actual stress and ultimate stress is replaced by the ratio between actual strain and allowable strain.
- The allowable strain is set to  $5 \cdot 10^{-3}$ , see Subsection 7.1.
- There is no fatigue limit; the S-N curve is monotonously decreasing.
- S-N curves with a stress ratio of 0.1 are taken as reference, analogous to the stress ratio of the D150 configuration.
- Since a scatter of cycle numbers, at which failures occur, is observed in the fatigue experiments, a safety factor of 10 is assumed for the strain cycles to failure.
- Strain amplifications due to structural discontinuities are not considered.

With those assumptions, the approximation function for the S-N curve is:

$$N_f = \left( \frac{\epsilon_{rel}}{C} \right)^n \cdot \frac{1}{F_S}, \quad (17)$$

with:

$$\epsilon_{rel} = \frac{\epsilon_{1,max}}{\epsilon_{ult}} = \frac{2\epsilon_{1,a}}{\epsilon_{ult} (1 - r_s)} \quad (18)$$

and the number of cycles to failure  $N_f$ , the relative strain  $\epsilon_{rel}$ , the S-N curve coefficient  $C$  of 1.037, the S-N curve exponent  $n$  of  $-30.59=1/-0.03269$ , the safety factor  $F_S$ , the maximum major principal strain  $\epsilon_{1,max}$ , the ultimate strain  $\epsilon_{ult}$  of  $5 \cdot 10^{-3}$ , the major principal strain amplitude  $\epsilon_{1,a}$  and the strain ratio  $r_s$ .

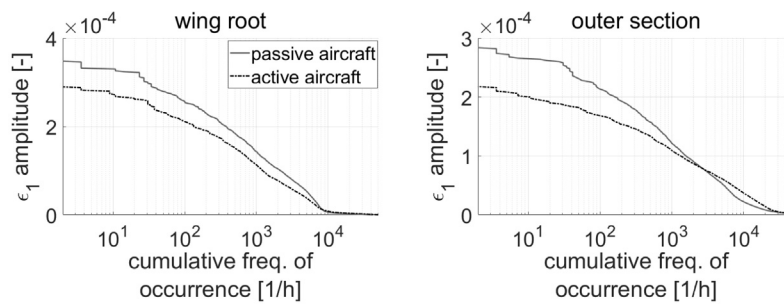


Fig. 18. Strain collectives of ALLEGRA during climb.

Table 7

Turbulence fatigue damage per flight - ALLEGRA.

Observed shell element	Damage per flight:	
	passive aircraft	active aircraft
Wing root	$2.74 \cdot 10^{-23}$	$4.49 \cdot 10^{-26}$
Outer section	$2.83 \cdot 10^{-26}$	$9.36 \cdot 10^{-30}$
HTP root	$6.24 \cdot 10^{-34}$	$2.26 \cdot 10^{-33}$

Table 8

Fatigue damage per ground-air-ground cycle - ALLEGRA.

Observed shell element	Damage per flight:	
	passive aircraft	active aircraft
Wing root	$5.77 \cdot 10^{-24}$	$2.97 \cdot 10^{-23}$
Outer section	$5.18 \cdot 10^{-25}$	$1.24 \cdot 10^{-24}$
HTP root	$3.40 \cdot 10^{-38}$	$4.31 \cdot 10^{-38}$

Table 9

Fatigue damage per flight cycle - ALLEGRA.

Observed shell element	Damage per flight:	
	passive aircraft	active aircraft
Wing root	$3.32 \cdot 10^{-23}$	$2.97 \cdot 10^{-23}$
Outer section	$8.01 \cdot 10^{-25}$	$1.24 \cdot 10^{-24}$
HTP root	$6.24 \cdot 10^{-34}$	$2.26 \cdot 10^{-33}$

Table 7 lists the turbulence damage for one reference flight mission according to Table 6. Table 8 lists the fatigue damage per ground-air-ground cycle obtained from the loads during a +1.3 g maneuver. An addition of the values from Table 7 and Table 8 yields the total fatigue damage in one flight, see Table 9.

With the fatigue damage values in Table 7, Table 8 and Table 9, it is concluded that:

- In turbulence, there is a clear tendency that the wing of the active aircraft shows significantly less fatigue damage compared to the passive aircraft. However, the HTP of the active aircraft receives slightly more damage. This is caused by the GLA evoking a small amount of pitching moments due to the aileron deflections. This results in the pitching acceleration on the active aircraft being up to 2.2% higher (in terms of root mean square). This in turn causes additional vertical movements and also loads at the HTP.
- One ground-air-ground cycle causes higher fatigue damage values on the wing of the active aircraft compared to the passive aircraft. On the passive aircraft, the ground-air-ground cycle causes up to 17% of the total fatigue damage. On the active aircraft, more than 99% of the total fatigue damage is inflicted by the ground-air-ground cycle.
- In general, the wing root receives more fatigue damage compared to the outer wing section.

- Judging by the highest damage values of each aircraft (the largest numbers in every column in Table 9) which are  $3.32 \cdot 10^{-23}$  on the passive and  $2.97 \cdot 10^{-23}$  on the active aircraft, the expected fatigue life of the active aircraft is 1.12 times longer than the passive counterpart.

If the fatigue damage values listed in Table 9 are accumulated for e.g. 40000 flight cycles, those are still significantly below 1.0, assuming that the turbulence RMS is equal to the values in Table 6 and there is no strain amplification due to structure discontinuities.

## 8. Conclusions

The described method provides an insight into the effects of load alleviation on the design loads, mass reduction and the resulting change in the fatigue behavior of a given aircraft in the pre-design phase before it advances to the next design stage. The analyses cover multiple disciplines (loads, aeroelasticity, aerodynamics, structure, flight mechanics, control theory, fatigue) and can help in understanding the interdependencies between each involved discipline.

Concerning the wing structural mass reduction on the backward swept D150 configuration, 130.5 kg (0.18% of MTOM, 0.32% of OEM) can be saved in total. On the forward swept ALLEGRA configuration, the wing mass decrease is 410.4 kg (0.56% of MTOM, 0.94% of OEM). As a comparison: Wildschek et al. [19] stated in 2013 that on a large blended wing-body configuration, load alleviation using a feed-forward  $L_\infty$ -optimal control can yield a mass reduction by 0.5% of the maximum take-off mass. A further reference is the active load alleviation system on the Lockheed C-5A [1] documented in 1976. The system was initially developed to extend the fatigue life of the structure, however it was discarded and a structural modification was introduced. The structural modification increased the empty mass of the aircraft by 5.5%. However, it cannot be concluded that the active load alleviation can yield that mass reduction since the structure of the C-5A is not likely to be completely re-optimized after discarding the load alleviation.

Concerning fatigue, no comparison with literature results could be made since no data of fatigue comparisons with a separate optimization of the active aircraft could be found. If load alleviation functions are implemented without updating the structure, the fatigue benefits are expected to be higher compared to Subsection 6.3 and 7.3. On the Lockheed C-5A, the active load alleviation yields a fatigue life improvement of 25-50% [32] in 1977. On a business jet configuration investigated by Paletta [4] in 2011, the fatigue life is extended by 44-67%.

In addition, the following aspects are seen as worth mentioning:

- An implementation of load alleviation can reduce the flight loads, wing structural mass and extend the wing's fatigue life in turbulent weather. For ground-air-ground cycles, the wing

of the active aircraft tends to receive more fatigue damage than a passive one. Overall however, the active aircraft show fatigue life improvement compared to the passive counterpart.

- With the current fatigue analysis method, a comparative analysis between the active and passive aircraft is possible. For absolute numbers of the fatigue damage values however, more detailed FE models including the stress/strain amplification factors are necessary.

There are several potential aspects that could be considered in the future. The first one concerns the design load calculations. In this aspect, the load case variety can be extended to reproduce the design load cases of a certified aircraft as close as possible. For the wing, this includes landing, roll and asymmetric load cases as well as gust cases with extended airbrakes. Regarding the aerodynamics in the transonic regime, reduced order models that are based on CFD as shown by Bekemeyer et al. [33] and Li et al. [34] can be taken into account. Furthermore, flight mechanical control can be implemented in the gust simulations, as shown by Voß [35]. In the fatigue analysis, further flight missions as well as a probability distribution of turbulence intensities can be considered to have a more realistic model of an aircraft's service life.

#### Declaration of competing interest

The authors declare that they have no known competing financial interests or personal relationships that could have appeared to influence the work reported in this paper.

#### References

- [1] C. Regan, C. Jutte, Survey of Applications of Active Control Technology for Gust Alleviation and New Challenges for Lighter-weight Aircraft, Technical Report, Dryden Flight Research Center, Edwards, California, 2012.
- [2] S. Binder, A. Wildschek, R. De Breuker, The interaction between active aeroelastic control and structural tailoring in aeroservoelastic wing design, *Aerosp. Sci. Technol.* 110 (2021).
- [3] J. Xu, I. Kroo, Aircraft design with active load alleviation and natural laminar flow, *J. Aircr.* 51 (2014).
- [4] N. Paletta, Maneuver Load Controls, Analysis and Design for Flexible Aircraft, Doctoral thesis, University of Naples Federico II, Napoli, 2011.
- [5] P. Teufel, Böenmodellierung und Lastabminderung für ein flexibles Flugzeug, Doctoral thesis, Universität Stuttgart, Stuttgart, 2003.
- [6] V. Handojo, Contribution to Load Alleviation in Aircraft Pre-design and Its Influence on Structural Mass and Fatigue, DLR-Forschungsbericht, DLR-FB-2020-47, Dissertation, Technische Universität Berlin, 2021.
- [7] T. Zill, P. Ciampa, B. Nagel, Multidisciplinary Design Optimization in a Collaborative Distributed Aircraft Design System, 2012.
- [8] A. Seitz, M. Kruse, T. Wunderlich, J. Bold, L. Heinrich, The DLR Project LamAir: Design of a NLF Forward Swept Wing for Short and Medium Range Transport Application, 2011.
- [9] T. Klimmek, Parametric set-up of a structural model for FERMAT configuration for aeroelastic and loads analysis, *ASD J.* 3 (2014).
- [10] T. Klimmek, Statische aeroelastische Anforderungen beim multidisziplinären Strukturwurf von Verkehrsflugzeugflügeln, Doctoral thesis, Technische Universität Braunschweig, Braunschweig, 2016.
- [11] E. Albano, W. Rodden, A doublet lattice method for calculating lift distributions on oscillating surfaces in subsonic flows, *AIAA J.* 7 (1968).
- [12] MSC Corporation, MSC Nastran Version 68 - Aeroelastic Analysis User's Guide, Technical Report, 2014.
- [13] J. Giesing, T. Kálmán, W. Rodden, Subsonic steady and oscillatory aerodynamics for multiple interfering wings and bodies, *J. Aircr.* 9 (1972).
- [14] European Aviation Safety Agency, CS25 - Certification Specifications and Acceptable Means of Compliance for Large Aeroplanes, Amendment 23.
- [15] MSC Corporation, MSC Nastran 2012 - Design Sensitivity and Optimization User's Guide, Technical Report, 2011.
- [16] H. Ramsey, J. Lewolt, Design Maneuver Loads for an Airplane with an Active Control System, 1979.
- [17] R. König, K. Hahn, Load alleviation and ride smoothing investigations using ATTAS, in: *Proceeding of the 17th ICAS*, 1990.
- [18] H. Schlichting, E. Truckenbrodt, *Aerodynamik des Flugzeuges*, zweiter Band, Springer, Berlin, Heidelberg, New York, 1969.
- [19] A. Wildschek, An Adaptive Feed-Forward Controller for Active Wing Bending Vibration Alleviation on Large Transport Aircraft, Doctoral thesis, Technische Universität München, München, 2008.
- [20] Fuelplanner, <http://fuelplanner.com/index.php>. (Accessed 31 July 2018). Online.
- [21] Joint aviation authorities, JAR-OPS 1, <http://www.edkb.de/Download%20Angebote/JAR-OPS1.pdf>. (Accessed 31 July 2018). Online.
- [22] U. D. of Defense, MIL-STD-1797A - Flying Qualities of Piloted Aircraft Notice 3, Technical Report, 2004.
- [23] A. Nieslony, Rainflow counting algorithm, <https://de.mathworks.com/matlabcentral/fileexchange/3026-rainflow-counting-algorithm>. (Accessed 5 October 2018). Online.
- [24] A. Payne, The fatigue of aircraft structures, *Eng. Fract. Mech.* 8 (1976).
- [25] Federal Aviation Administration, Statistical Loads Data for the Airbus A-320 Aircraft in Commercial Operations, Technical Report DOT/FAA/AR-02/35, 2002.
- [26] A. Ekberg, Palmgren - Miner's rule, <http://www.am.chalmers.se/~anek/teaching/fatfract/98-4.pdf>. (Accessed 5 October 2018). Online.
- [27] G. Pinho Chiozzotto, Improving Aircraft Conceptual Design with Methods for Wing Loads, Aeroelasticity and Mass Estimation, Doctoral thesis, Technische Universität Berlin, Berlin, 2017.
- [28] H. Mayer, R. Schuller, M. Fitzka, Fatigue of 2024-T351 aluminium alloy at different load ratios up to  $10^{10}$  cycles, *Int. J. Fatigue* 57 (2013).
- [29] S. Ijsselmuiden, Optimal Design of Variable Stiffness Composite Structures Using Lamination Parameters, Doctoral thesis, Delft University of Technology, Delft, 2011.
- [30] R. Tetlow, Design Charts for Carbon Fibre Composites, Technical Report, Cranfield Institute of Technology, Cranfield, 1970.
- [31] X. Tan, E. Armanios, An assessment of fatigue limit predictors of graphite/epoxy co-cured composite joints through quasi-static acoustic emission count peaks, in: *Fatigue of Composite Materials*, vol. 3, 2013.
- [32] T. Disney, C-5A active load alleviation system, *J. Spacecr. Rockets* 14 (1977).
- [33] P. Bekemeyer, S. Timme, Flexible aircraft gust encounter simulation using sub-space projection model reduction, *Aerosp. Sci. Technol.* 86 (2019).
- [34] D. Li, A. Da Ronch, G. Chen, Y. Li, Aeroelastic global structural optimization using an efficient CFD-based reduced order model, *Aerosp. Sci. Technol.* 94 (2019).
- [35] A. Voß, Open and closed loop gust loads analyses for a flying wing configuration with variable longitudinal stability, *Aerosp. Sci. Technol.* 89 (2019).